Enhancing Surface Plasmon Detection Using Template-Stripped Gold Nanoslit Arrays on Plastic Films

Kuang-Li Lee,[†] Pei-Wen Chen,[‡] Shu-Han Wu,[§] Jhih-Bin Huang,[‡] Sen-Yeu Yang,[∥] and Pei-Kuen Wei[†,§,⊥,*]

[†]Research Center for Applied Sciences, Academia Sinica, 128, section 2, Academia Road, Nangkang, Taipei 11529, Taiwan, [‡]Department of Mechanical and Mechatronic Engineering, National Taiwan Ocean University, Keelung, Taiwan, [§]Institute of Biophotonics, National Yang-Ming University, Taipei, Taiwan, [⊥]Department of Optoelectronics, National Taiwan Ocean University, Keelung, Taiwan, and [∥]Department of Mechanical Engineering, National Taiwan University, Taipei, Taiwan

ABSTRACT

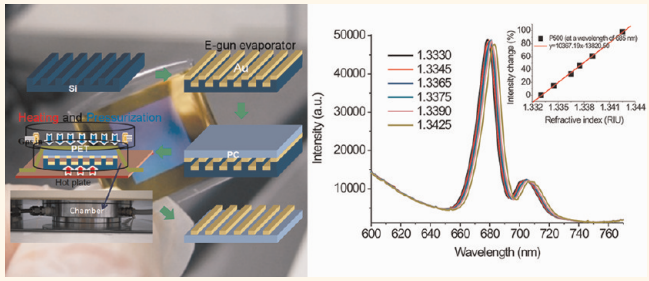

Nanostructure-based sensors are capable of sensitive and label-free detection for biomedical applications. However, high-throughput and low-cost fabrication techniques are the main issues which should be addressed. In this study, chip-based nanostructures for intensity-sensitive detection were fabricated and tested using a thermal-annealing-assisted template-stripping method. Large-area uniform nanoslit arrays with a 500 nm period and various slit widths, from 30 to 165 nm, were made on plastic films. A transverse magnetic-polarized wave in these gold nanostructures generated sharp and asymmetric Fano resonances in transmission spectra. The full width at half-maximum bandwidth decreased with the decrease of the slit width. The narrowest bandwidth was smaller than 10 nm. Compared to nanoslit arrays on glass substrates using electron-beam lithography, the proposed chip has a higher intensity sensitivity up to 10367%/RIU (refractive index unit) and reaches a figure of merit up to 55. The higher intensity sensitivity for the template-stripped nanostructure is attributed to a smoother gold surface and larger grain sizes on the plastic film, which reduces the surface plasmon propagation loss.

KEYWORDS: surface plasmon resonance · subwavelength structures · optical sensors · template stripping · nanoslit array · Fano resonance

Surface plasmon resonance (SPR) sensing is a real-time and label-free detection technique to measure biomolecular interactions on a gold surface.[1−3] The most common method to induce SPR on the gold surface is to utilize an optical prism, known as the Kretschmann configuration. On the basis of this SPR excitation technique, commercial BIAcore instruments enable real-time and label-free measurements of biomolecular binding affinity. In addition to the prism coupling method, the SPR can also be excited using metallic nanostructures.[4−7] Biosensors based on extraordinary transmission of periodic nanohole arrays or nanoslit arrays in gold have been proposed.[8−15] Compared to the prism-based SPR sensors, gold nanostructures take advantage of small detection volume and a normal light incidence condition. They provide a feasible way to achieve chip-based, high-throughput, and label-free detection for modern DNA and protein microarrays.[16,17] In periodic metallic nanostructures, the extraordinary transmission is usually accompanied by an asymmetric resonant spectrum. This observed Fano-like resonance profile is understood in terms of the coupling of the surface-bound state of a periodic array (a discrete state) with the incoming wave (a continuum state).[18−20] The former is associated with Bloch wave surface plasmon polariton (BW-SPP) in periodic nanostructures. For normally incident light, the BW-SPP condition for one-dimensional periodic structures is described by

$$\lambda_{SPR}(n, i) = \frac{p}{i}\left(\frac{\varepsilon_m n^2}{\varepsilon_m + n^2}\right)^{1/2} \quad (1)$$

where i is the resonant order, P is the period of the nanostructure, ε_m is the dielectric constant of the metal, and n is the environmental refractive index. The resonant wavelength is red-shifted when the refractive index of the medium near the gold surface changes. In general, the wavelength sensitivity, $\Delta\lambda_{SPR}/\Delta n$, is proportional to the period. Increasing the period can increase the wavelength sensitivity. However, for real-time and high-throughput applications,

* Address correspondence to pkwei@gate.sinica.edu.tw.

Received for review October 17, 2011 and accepted March 27, 2012.

Published online March 27, 2012
10.1021/nn3001142

the change of transmission intensity at a fixed wavelength is often employed as the signal. The intensity sensitivity is defined as $(\Delta I/I_0)/\Delta n$, where $\Delta I/I_0$ is the normalized intensity change. It is determined by both the wavelength sensitivity and resonant bandwidth. The figure of merit (FoM) of metallic nanostructures in wavelength units is defined as $(\Delta\lambda_{SPR}/\Delta n)/\Delta\lambda$, where $\Delta\lambda$ is the full width at half-maximum (fwhm) bandwidth. The fwhm is related to the loss of SPR. It is dependent on gold film properties and would be different from different fabrication processes.

The majority of the fabrication techniques for gold nanostructures utilize focused ion beam (FIB) milling to directly pattern gold films or electron-beam lithography (EBL) combined with a dry etching method or a lift-off process to generate a nanostructure on a substrate. However, these writing techniques are not suitable for massive production. Besides, the gold film made from the vacuum deposition leads to higher SPR loss due to the scattering of electrons at gold grain boundaries. To solve the mass-fabrication problem, many groups have proposed interference lithography,[21] nanoimprint lithography,[22] nanosphere lithography,[23] and soft lithography techniques,[24] *etc*. To solve the SPR loss problem, the gold film can be annealed at an elevated temperature to form large gold grains.[25,26] Recently, a mass-fabrication process for making high-quality metallic nanostructures was proposed by using a thermal-annealing and template-stripping method.[25,27−29] It does not require additional etching or lift-off processes. Typically, a metallic film is coated on the patterned silicon template. The exposed surface of the metal is then attached to another substrate with an epoxy adhesive. The optical epoxy acts as an adhesion layer to attach the metallic film to a clean substrate. It has to be cured thermally or with ultraviolet light. After peeling off from the template, a smooth gold or silver surface with larger grain sizes on the epoxy film is obtained.[25,29] Such template-stripped gratings can have very sharp line widths (~10 nm) in the reflection spectrum.[29] In this paper, we utilized a thermal-annealed template-stripping method to fabricate large-area gold nanoslit arrays on plastic films with low cost and high SPR sensitivities. The gold film coated on the patterned silicon template was directly imprinted on the plastic film at a temperature higher than the glass transition temperature of the plastic film. The gold nanostructures are embedded on the plastic film after peeling off from the silicon template. This approach makes use of the poor adhesion of noble metals on the silicon template and good adhesion to the softened plastic film. It does not require additional epoxy and UV cure processes. It is simpler and also produces smooth gold surface and larger grain sizes. In this work, gold nanoslit arrays with a 500 nm period and various slit widths, from 30 to 165 nm, were made and tested using the intensity interrogation method. We found that a transverse magnetic (TM)-polarized wave in these gold nanostructures generated sharp and asymmetric Fano resonances in transmission spectra. The fwhm values of Fano resonances decreased with the decrease of the slit width, and the narrowest bandwidth was smaller than 10 nm. The thermal-annealed template-stripping SPR sensor can reach an intensity sensitivity of up to 10367%/RIU and a FoM of up to 55. This value is much higher than those of previous nanoslit and nanohole arrays fabricated by the EBL and FIB methods. From atomic force microscopy (AFM) images, we confirm that such an enhanced intensity sensitivity for the template-stripped nanoslit array is attributed to a smoother gold surface and larger grain sizes during the thermal-annealing process. It results in a decrease of surface plasmon propagation loss.

RESULTS AND DISCUSSION

Figure 1a shows the measured transmission spectra of the 500 nm period, 30 nm wide nanoslit array in air and water for normally incident TM-polarized light. The TM-polarized light with E and k vectors *versus* the structures is depicted in the inset. There are transmission peaks and dips in the spectrum due to the couplings of direct slit transmission (or localized surface plasmon resonance (LSPR) in the nanoslits) and BW-SPPs on the periodic metal surface. The interaction between direct slit transmission (a continuum state) and BW-SPPs (a discrete state) creates a Fano-like resonance profile consisting of a minimum, close to the position predicted by eq 1, and an adjacent maximum. A sharp Fano-like resonance was observed in air. The corresponding peak and dip wavelengths for the Fano resonance were 796 and 809 nm, respectively. From eq 1, the resonant wavelength of the BW-SPP is 832 nm at the PC/gold interface ($\varepsilon_m = -29 + 2.0i$ for gold at 800 nm, $i = 1$, $n = 1.584$, and $P = 500$ nm). Obviously, the experimental wavelength was close to the theoretical wavelength. It is noted from eq 1 that the resonant wavelength of the BW-SPP for the 500 nm period array is 550 nm at the air/gold interface ($\varepsilon_m = -5.8 + 2.1i$ for gold at 549 nm, $n = 1$ and $P = 500$ nm). The expected resonance at the air/gold interface is not found due to the large propagation loss of surface plasmons at this wavelength. Gold is a highly dispersive material; the SPR propagation constant (k_{SPR}) is strongly dependent on the wavelength (λ_{SPR}) and can be calculated by the following equation

$$k_{SPR} = \frac{2\pi}{\lambda_{SPR}}\sqrt{\frac{(\varepsilon_m n^2)}{(\varepsilon_m + n^2)}} \qquad (2)$$

At λ_{SPR} = 700 nm (the water/gold interface, P = 500 nm, $\varepsilon_m = -16.8 + 1.1i$, $n = 1.3320$), the propagation constant is $9.2544 + 0.0191i$ (1/μm). The propagation constant changes to $12.3891 + 0.4029i$ (1/μm) when

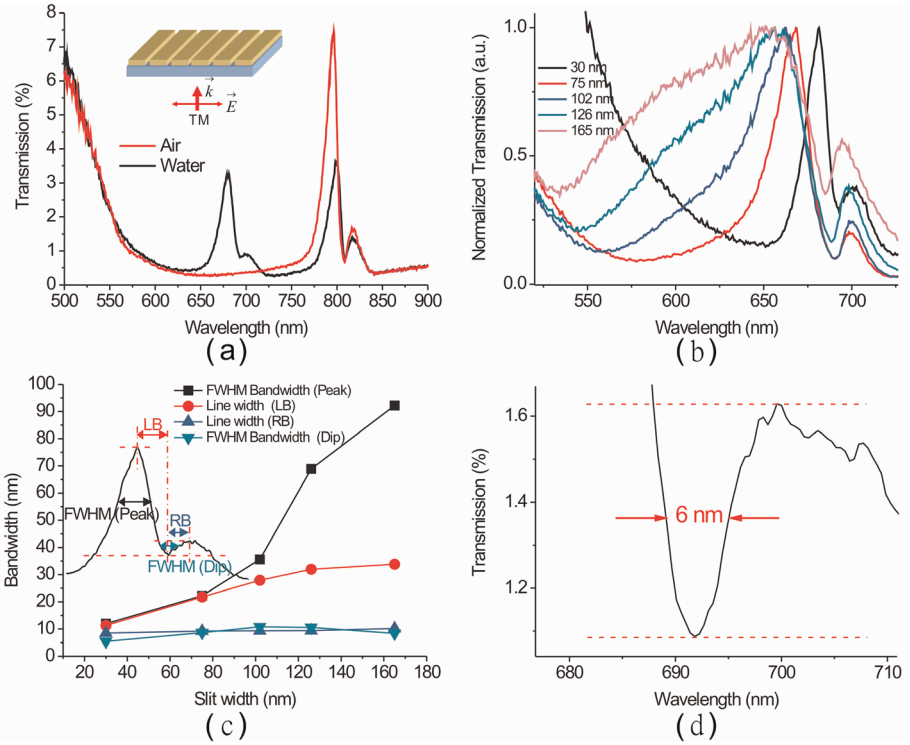

Figure 1. (a) Measured transmission spectra of the 500 nm period, 30 nm wide nanoslit array in air and water for normally incident TM-polarized light. The inset depicts the TM-polarized light with E and k vectors *versus* the structures. (b) Normalized transmission spectra of 500 nm period nanoslit arrays with various slit widths. The slit widths are from 30 to 165 nm. (c) Bandwidth of Fano resonance dip or peak as a function of the slit width. The inset depicts the definitions of the fwhm bandwidths, "Peak" and "Dip", and line widths, "LB" and "RB". Both the fwhm bandwidths and the line widths are compared. (d) Measured fwhm bandwidth of the Fano resonance dip at the water/gold interface for 30 nm wide nanoslit array. The fwhm bandwidth was 6 nm.

λ_{SPR} = 550 nm (the air/gold interface, $\varepsilon_m = -5.8 + 2.1i$, n = 1). Comparing the imaginary part of the SPR propagation constants, the propagation loss in air (λ_{SPR} = 550 nm) is 25.8 times higher than that in water (λ_{SPR} = 700 nm). Therefore, the BW-SPP mode at the air/gold interface is not obvious for the 500 nm period array. When the array was covered with water, there were two Fano resonances in the water spectrum. The resonant dip of Fano resonance at the water/gold interface was at the wavelength of 694 nm. The resonant dip of Fano resonance at the PC/gold interface remained unchanged. From eq 1, the resonant wavelength of the BW-SPP at the water/gold interface is 704 nm ($\varepsilon_m = -16.8 + 1.1i$ for gold at 705 nm, i = 1, n = 1.3320, and P = 500 nm). It is close to the experimental wavelength. For the Fano-type resonance, the resonant profile was also affected by the slit width. Figure 1b shows the normalized transmission spectra of 500 nm period nanoslit arrays with various slit widths. The slit widths ranged from 30 to 165 nm. It is obvious that as the slit width increases, the resonant peak or dip is blue-shifted and the bandwidth increases. The bandwidth of the Fano resonance dip or peak as a function of the slit width is shown in Figure 1c, and the inset depicts the definitions of fwhm bandwidths. For a 165 nm wide nanoslit array, the fwhm bandwidth of the Fano resonance peak near the wavelength of 655 nm was 92 nm. Taking the line width from the resonant peak to dip, the bandwidth was 34 nm. When the slit width was decreased to 30 nm, the bandwidths were 12 and 11 nm for the fwhm bandwidth and the line width from the peak to dip, respectively. Moreover, considering the bandwidth of Fano resonance dip, we found that the narrowest bandwidths for the fwhm bandwidth and the line width from the dip to peak were down to 6 nm (see Figure 1d) and 9 nm, respectively. Utilizing the proposed fabrication technique, the nanoslit arrays with sharper Fano resonances were made.

The uniformity of a large-area nanostructure is another important issue for high-throughput applications. We examined the uniformity of large-area nanoslit arrays. Figure 2a shows the measured transmission spectra of a 1 cm × 1 cm nanoslit array with a 500 nm period and 30 nm slit width in water for normally incident TM-polarized light. The spectra were measured at nine different positions of the nanoslit array. Figure 2b,c shows the resonant wavelengths and fwhm bandwidths of Fano resonances at the water/gold and substrate/gold interfaces as a function of the sample position. The fwhm bandwidths of the Fano resonance peak and dip at the water/gold interface

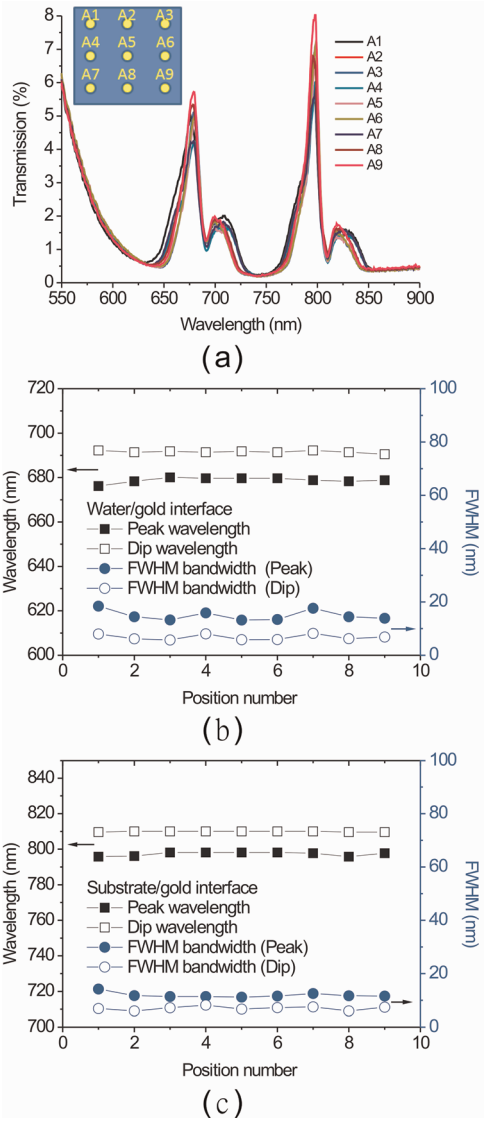

Figure 2. (a) Measured transmission spectra of the large-area nanoslit array with a 500 nm period and 30 nm slit width in water for normally incident TM-polarized light. (b) Resonant wavelengths and fwhm bandwidths of the Fano resonance at the water/gold interface as a function of the sample position. The mean values for the resonant wavelengths and fwhm bandwidths of the Fano resonance peak and dip at the water/gold interface are 678.8, 691.6, 14.9, and 6.78 nm, respectively. (c) Resonant wavelengths and fwhm bandwidths of Fano resonance at the substrate/gold interface as a function of the sample position. The mean values for the resonant wavelengths and fwhm bandwidths of the Fano resonance peak and dip at the substrate/gold interface are 797.3, 809.9, 11.9, and 7.02 nm, respectively.

(at the substrate/gold interface) were 14.9 nm (11.9 nm) and 6.78 nm (7.02 nm), respectively. The mean values for the resonant wavelengths of the Fano resonance peak and dip at the water/gold interface (at the substrate/gold interface) are 678.8 nm (797.3 nm) and 691.6 nm (809.9 nm), respectively. The standard deviation values for the resonant wavelengths and the fwhm bandwidths of the Fano resonance peak and dip at the water/gold interface (at the substrate/gold interface) are 1.18 nm (1.08 nm), 0.534 nm (0.197 nm), 1.95 nm (0.943 nm), and 1.02 nm (0.706 nm), respectively. From the above experiment, it is shown that large-area uniform nanostructures can be made using the thermal-annealing-assisted template-stripping method.

Bulk Sensitivity Test. To verify the high sensitivities of sensors fabricated by the thermal-annealed template-stripping method, we also compared nanoslit-based sensors on a glass substrate made by electron-beam lithography combined with a dry etching technique.[12] Both samples had the same 500 nm period, 60 nm wide, and 50 nm deep nanoslit arrays. The bulk sensitivities of these sensors were measured by injecting purified water mixed with various ratios of glycerin into the microfluidic devices. Figure 3a shows the measured transmission spectra of the 500 nm period nanoslit arrays in water for normally incident TM-polarized light. There are Fano-like resonance profiles in the spectra. Both wavelengths of Fano resonances at the water/gold interface are near 675 nm. Obviously, the template-stripping sample has a higher transmission and sharper Fano resonances. Moreover, the resonant wavelengths are red-shifted for the template-stripping sample. The Fano resonance is the inference between broad-band LSPR and BW-SPP. The LSPR is related to the gap plasmon in the nanoslits. For the proposed thermal-annealed template-stripping method, polycarbonate polymer is embedded in the nanoslit. It increases the refractive index in the slit (n = 1.582). The gap plasmon propagation loss is reduced in the nanoslits due to the increase of the dielectric constant. Therefore, a higher transmission was measured compared to gold nanoslits made by electron-beam lithography (see Figure 3a). From the Fabry–Perot model for the nanoslit,[30] the resonant wavelength can be estimated by

$$\lambda_0 = (4\pi n_{\text{eff}} h)/(2\pi - \varphi_1 - \varphi_2) \qquad (3)$$

where n_{eff} is the equivalent refractive index, h is the thickness of the gold film, and ϕ_1 and ϕ_2 are the phase shifts at the top and bottom interfaces, respectively.

The increase of the refractive index in the slit increased the LSPR wavelength. Therefore, the Fano resonance for the template-stripping sample occurs at a longer wavelength than the EBL sample. Figure 3b depicts the intensity spectra of the two kinds of nanoslits with various water/glycerin mixtures for normally incident TM-polarized waves. When the concentrations of glycerin increased, the wavelengths of Fano resonances were red-shifted and the intensities changed. Figure 3c,d shows the maximum intensity change and resonant wavelength against the refractive index of the outside medium for both samples. The slopes of the fitting curves show that the intensity sensitivities (wavelength sensitivities) were 5226%/RIU (451 nm/RIU) and 7615%/RIU (431 nm/RIU) for the dry etching and template-stripping methods, respectively.

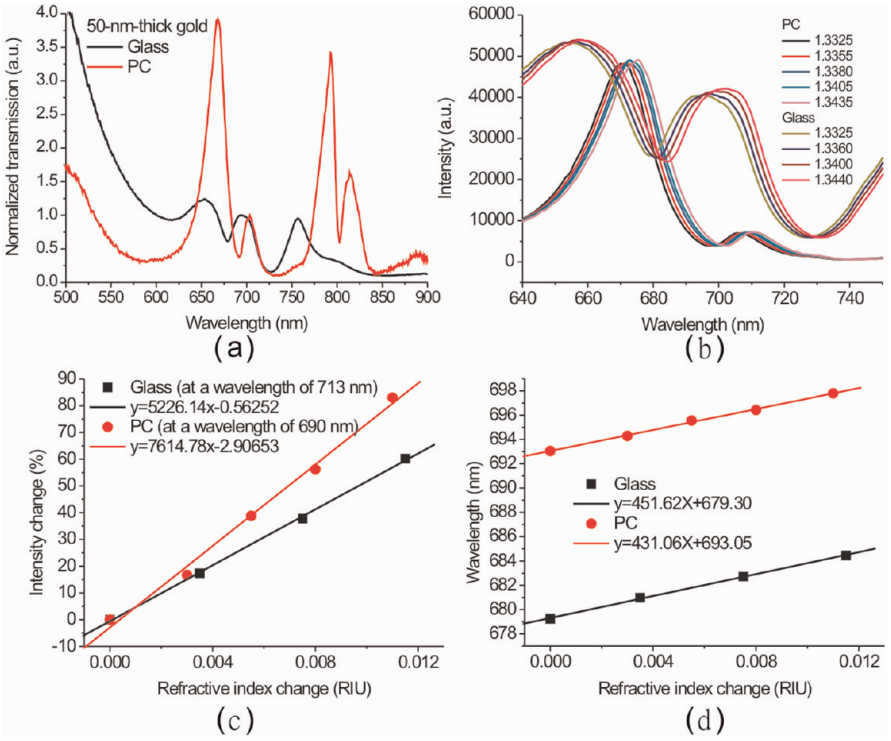

Figure 3. Refractive index sensing capabilities of the 500 nm period, 60 nm wide nanoslits made by the dry etching and template-stripping methods. (a) Measured transmission spectra of the 500 nm period nanoslit arrays made by both methods in water for normally incident TM-polarized light. (b) Intensity spectra of the nanoslits made on a glass substrate and a PC substrate with various water/glycerin mixtures for a normally incident TM-polarized wave. (c) Intensity change against the refractive index of the outside medium. The slopes of the fitting curves show that the refractive index sensitivities were 5226 and 7615%/RIU for the dry etching and template-stripping methods, respectively. (d) Resonant wavelength against the refractive index of the outside medium. The slopes of the fitting curves show that the wavelength sensitivities were 451 and 431 nm/RIU for the dry etching and template-stripping methods.

Obviously, the wavelength sensitivity is slightly reduced for the template-stripping sample because the nanoslit is occupied with the polymer. However, if we consider the improvement of the gold film quality, the low propagation loss results in a low bandwidth and a high figure of merit. Therefore, the template-stripping sample has a higher intensity sensitivity compared with nanostructures made by EBL, as seen in Figure 3c.

It is noted that the intensity sensitivity for 60 nm wide nanoslits can be further improved by narrowing the slit width. Figure 4a presents the intensity spectra of the 500 nm period, 30 nm wide nanoslit array with various water/glycerin mixtures for normally incident TM-polarized waves. The inset shows that the measured fwhm bandwidth of the Fano resonance dip at the water/gold interface was 7.7 nm. When the outside medium was changed from water to water/glycerin mixtures, the Fano-like resonance profile near 685 nm was red-shifted. Figure 4b shows the resonant wavelength and energy against the refractive index of the outside medium. The slopes of the fitting curves show that refractive index sensitivities were 1.102 eV/RIU and 427 nm/RIU. Figure 4c shows the intensity change against the refractive index of the outside medium for the 30 nm wide nanoslit array. The slope of the fitting curve shows that the bulk intensity sensitivity was 10367%/RIU. The measured intensity sensitivity is much better than the reported intensity sensitivities of ~1010−7593%/RIU.[1,10,14,31] The current structure can achieve a detection limit of 1.93×10^{-5} RIU when the intensity resolution is 0.2%. To compare the refractive index sensing capability of the fabricated nanostructures with previous works, we also calculated the FoM values in wavelength units and energy units. The figure of merit in energy units (FoM_E) is defined as m (eV/RIU)/fwhm (eV), where m is the linear regression slope for the refractive index dependence and fwhm is the resonant width of the plasmon resonance.[32] In Figure 4a,b, the fwhm bandwidth of the Fano dip was 7.7 nm (fwhm = 0.0198 eV) and the wavelength sensitivity was 427 nm/RIU. Thus, the FoM (FoM_E) value of 55.5 (55.4) was obtained. Taking the line width from the resonant peak to dip, the bandwidth was 12.6 nm (0.0331 eV), and we arrive at a FoM of 33.9 (33.2). These values are better than that of the periodic nanostructure-based SPR sensors[24] and the LSPR sensors,[7,33−37] for example, the periodic gold nanohole arrays (FoM of 23),[24] various shapes of gold nanoparticles (FoM_E = 0.6−4.5),[7,33] and the reported plasmonic nanostructures and metamaterials with Fano-type resonances (a nonconcentric ring/disk cavity (FoM of 8.34),[34] plasmonic nanoparticle clusters (FoM of 10.6),[35] an

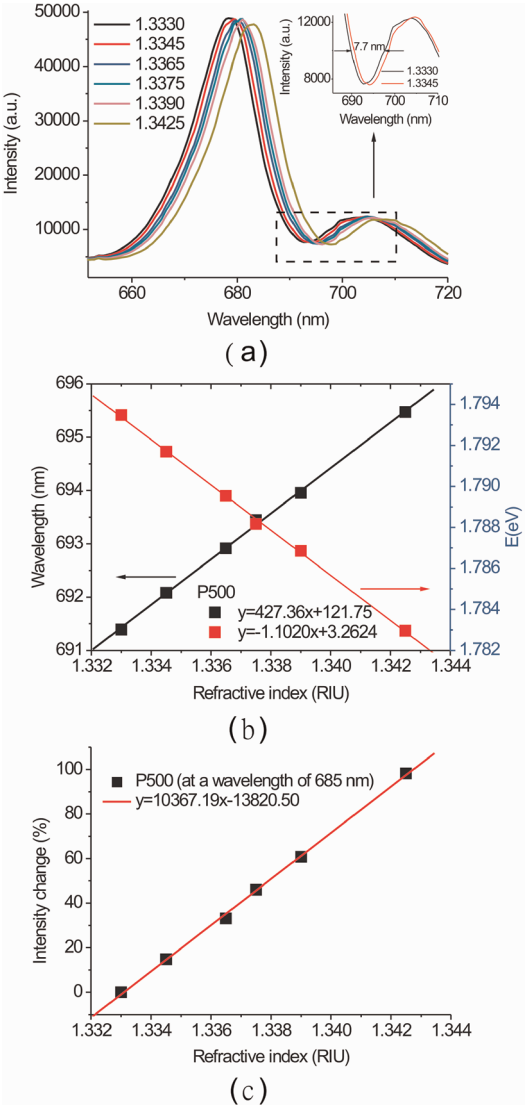

Figure 4. Refractive index sensing capabilities of the 500 nm period, 30 nm wide nanoslit array made by the template-stripping method. (a) Intensity spectra of the nanoslit array with various water/glycerin mixtures for a normally incident TM-polarized wave. The inset shows that the measured fwhm bandwidth of the Fano resonance dip at the water/gold interface was 7.7 nm. (b) Resonant wavelength and energy against the refractive index of the outside medium. The slopes of the fitting curves show that the refractive index sensitivities were 413 nm/RIU and 1.102 eV/RIU. (c) Intensity change against the refractive index of the outside medium. The slope of the fitting curve shows that the intensity sensitivity was 10367%/RIU.

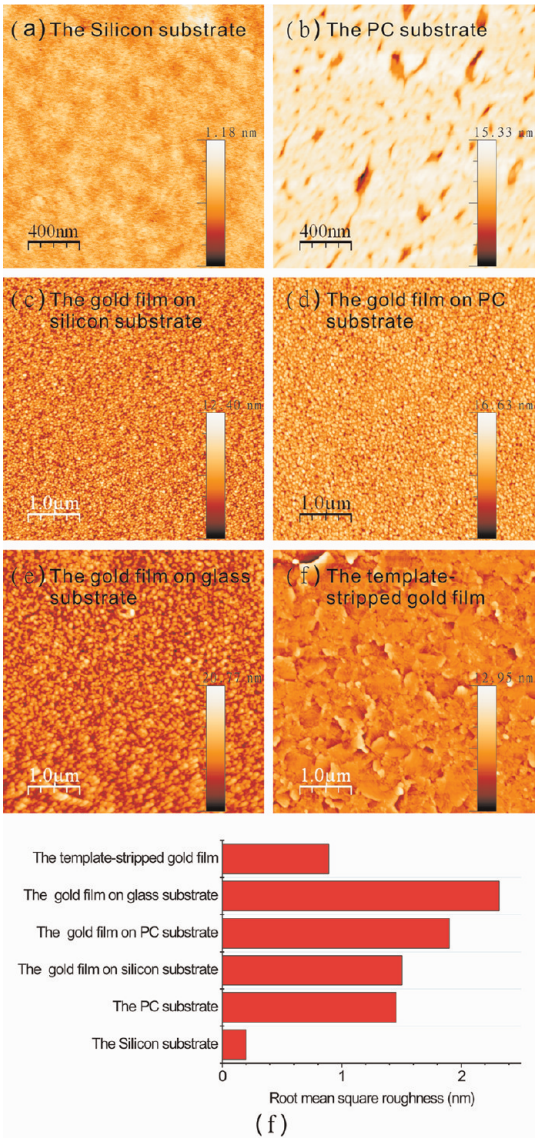

Figure 5. Atomic force microscopy images of the silicon template (a), the PC substrate (b), the 50 nm thick gold film on silicon template (c), on PC substrate (d), on glass substrate (e), and the template-stripped gold film on PC substrate (f). The grain size increased between (c) and (f) because the template-stripped film was annealed at 170 °C for 30 min during the fabrication process. (g) Root-mean-square roughness values extracted from the AFM images for these samples. The roughness of the template-stripped gold film is smaller than that of the gold film directly deposited on glass substrate, silicon substrate, or PC film.

electromagnetically induced transparency (EIT)-based planar metamaterial (FoM of 5.3),[36] and nano-cross-structures (FoM of 4.6)[37]).

The higher intensity sensitivity for the thermal-annealed template-stripped gold nanostructures is related to the smoother gold surface and larger grain sizes, which lead to a decreased imaginary dielectric constant of the gold film[25,26] and result in a narrower bandwidth. Figure 5a,b shows the AFM images of the silicon template and a PC substrate. Figure 5c–e depicts the AFM images of a 50 nm thick gold film on the silicon template, PC substrate, and glass substrate, respectively. Figure 5f shows the AFM image of a template-stripped gold film on the PC substrate. All of the root-mean-square (rms) roughnesses extracted from these AFM images are shown in Figure 5g for comparison. The rms roughness values were 0.199 nm (the silicon template), 1.45 nm (the PC substrate), 1.50 nm (the gold film on silicon template), 1.90 nm (the gold film on PC substrate), 2.31 nm (the gold film on glass substrate), and 0.890 nm (the template-stripped gold film). Obviously, the silicon template has the smoothest surface.

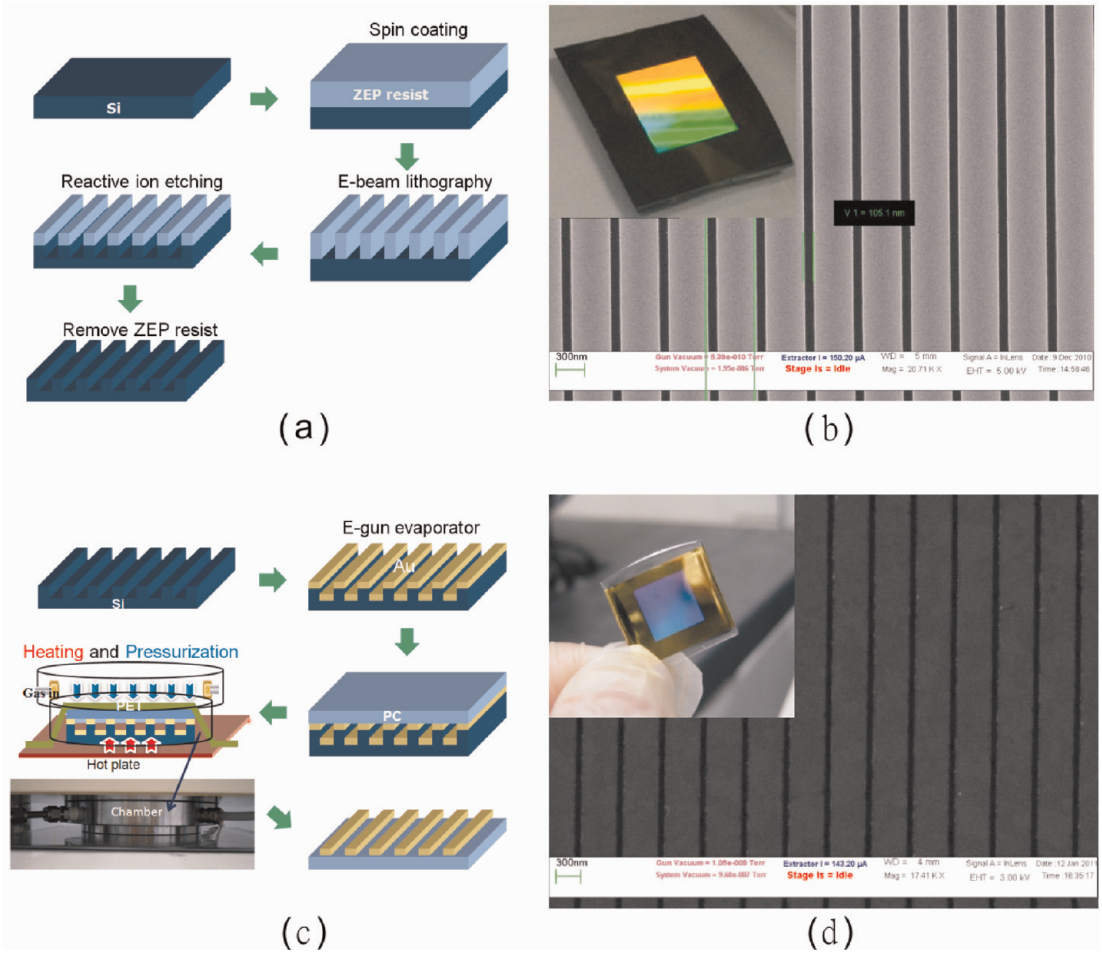

Figure 6. (a) Process flowchart for the fabrication of a silicon template. (b) SEM and optical images (inset) of the fabricated silicon template. The slit width is 105 nm, and the area of the slit array is 1 cm × 1 cm. (c) Process flowchart for the fabrication of metallic nanostructures. (d) SEM and optical images (inset) of the template-stripped nanoslits. The slit width is 60 nm, and the area of the slit array is 1 cm × 1 cm.

However, after the gold coating, the rms roughness is increased to 1.5 nm with many small gold grains on the surface. For the EBL method, the gold film deposited on the glass substrate has the roughest surface. Comparing the rms values of the gold film before and after thermal annealing and template stripping, we observed a great improvement on both the surface flatness and grain size. The surface roughness is reduced from 1.9 to 0.89 nm. We deduced that such large grains resulted from the annealed process at 170 °C for 30 min during the fabrication process. From the above AFM images and rms values, the higher intensity sensitivity for template-stripped nanostructures is due to the smoother gold surface and formation of larger grain sizes.

SUMMARY AND CONCLUDING REMARKS

We fabricated large-area uniform nanoslit arrays on a polycarbonate substrate for intensity-sensitive detection using a thermal-annealing-assisted template-stripping method. The experimental results show that TM waves in these gold nanostructures generated sharper Fano resonances in transmission spectra. The fwhm bandwidths of Fano resonances decreased with the decrease of the slit width, and the narrowest bandwidth was smaller than 10 nm. Compared to nanoslit arrays using EBL and a dry etching method, the proposed sensor has a higher intensity sensitivity of up to 10367%/RIU and reaches a figure of merit of up to 55. This value is better than SPR sensors using complicated two-dimensional gold nanostructures.[24] The higher intensity sensitivity for the template-stripped nanostructure is attributed to the smoother gold surface and larger grain sizes which lead to a decreased SPR loss. Currently, the wavelength sensitivity is 427 nm/RIU in the visible region. The highly sensitive sensors may also be achieved by using large-period nanoslits because the wavelength sensitivity is proportional to the period. However, when the period is increased to 1−2 μm, the resonant wavelength will be shifted to the near-infrared region.[9,38] The absorption in water will increase significantly, prohibiting optical transmission measurements. Therefore, the proposed method, increasing the intensity sensitivity by reducing the SPR loss, is more suitable for studying

bio−bio interactions in a water environment. Such inexpensive, reproducible, and high-throughput fabrication of large-area uniform nanoslit array chips can benefit sensing applications.

MATERIALS AND METHODS

Fabrication of Silicon Template. Large-area nanoslit arrays on a silicon substrate were fabricated using electron-beam lithography and a reactive ion etching method. Figure 6a depicts a process flowchart for the fabrication of a silicon template. A 300 nm thick ZEP-520 resist (ZEP-520, Zeon Corp, Tokyo, Japan) was spin-coated on a 525 μm thick silicon substrate. An electron-beam writer system (Elionix ELS 7000) was used to write large-area nanoslit arrays with various slit widths. The patterns were then transferred to the silicon substrate by using a reactive ion etching machine (Oxford Instrument, plasmalab 80plus). The power of the radio frequency (RF) electromagnetic wave in the reaction chamber was 150 W. The chamber pressure was 1×10^{-2} Torr, and the flow rates of CHF_3 and SF_6 gases were 50 and 25 sccm, respectively. The resist was removed by rinsing the sample in acetone for a few minutes before it was put in ultrapure water and purged dry by nitrogen. In the experiment, large-area nanoslit arrays with a 500 nm period, 150 nm depth, and various slit widths, from 50 to 180 nm, were made. Figure 6b shows the scanning electron microscope (SEM) and optical images (inset) of the fabricated silicon template. The slit width is 105 nm, and the area of the slit array is 1 cm $\times$ 1 cm.

Fabrication of Metallic Nanostructures. Large-area metallic nanostructures were made on a polycarbonate (PC) substrate using a thermal-annealing-assisted template-stripping method.[39] Figure 6c depicts a process flowchart for the fabrication of metallic nanostructures. A 50 nm thick gold film was deposited at a slow deposition rate (0.1 nm/s) on the clean silicon template using an electron gun evaporator. A 178 μm thick PC film (Lexan8010, GE, USA) was placed on the gold-coated template. The template and PC substrate were placed on a heating plate. It was heated at a temperature of 170 °C to soften the PC substrate. In the system, nitrogen gas was introduced into the chamber to produce a pressing pressure (2 kgw/cm^2) over the film. An additional polyethylene terephthalate (PET) thin film was used as the sealing film. It pressed the silicon mold and PC substrate with large-area uniformity. This step made the gold film uniformly stuck to the softened PC film. The template and substrate were then cooled and taken out from the chamber. As the gold film had a poor adhesion to the silicon template, the PC film was easily separated from the silicon template. After peeling off from the template and PET thin film, the PC substrate with metallic nanostructures was made. Figure 6d shows the SEM and optical images (inset) of the template-stripped nanoslits. The slit width was 60 nm, and the area of the slit array is 1 cm $\times$ 1 cm.

Optical Setup for Transmission Spectrum Measurement. The transmission spectra were measured by a simple optical transmission setup.[14] A 12 W halogen light was spatially filtered by using an iris diaphragm and a collimation lens. Its incident polarization was controlled by a linear polarizer. The white light was focused on a single array by using a 10$\times$ objective lens. The transmission light was collected by another 10$\times$ objective lens and focused on a fiber cable. The transmission spectrum was taken by using a fiber-coupled linear CCD array spectrometer (BWTEK, BTC112E). In the experiment, the metallic nanostructures were mounted on a microfluidic channel made from plexiglass. The refractive index sensitivities were measured by covering purified water mixed with various fractions of glycerin over the sample surface. The refractive indexes of the mixtures (from 0 to 15% glycerin) ranged from 1.3325 to 1.3435.

Atomic Force Microscopy (AFM) Measurements. All atomic force microscopy images were obtained with a Veeco di Innova AFM instrument operating in tapping mode in air. The scan size of the AFM image is typically 5 μm $\times$ 5 μm area at a scan rate of 0.8 Hz. All pf the root-mean-square roughness values were extracted from these AFM images.

Conflict of Interest: The authors declare no competing financial interest.

Acknowledgment. This work was supported by National Science Council, Taipei, Taiwan, under Contract No. NSC-100-2120-M-007-006 and NSC-100-2221-E-001-010-MY3. Technical support from NanoCore, the core facilities for nanoscience and nanotechnology at Academia Sinica in Taiwan, is acknowledged.

REFERENCES AND NOTES

1. Homola, J.; Yee, S. S.; Gauglitz, G. Surface Plasmon Resonance Sensors: Review. *Sens. Actuators, B* **1999**, *54*, 3–15.
2. Maier, S. A. Surface-Plasmon-Polariton-Based Sensors. In *Plasmonics: Fundamentals and Applications*; Springer Science: New York, 2007; pp 188−192.
3. Stewart, M. E.; Anderton, C. R.; Thompson, L. B.; Maria, J.; Gray, S. K.; Rogers, J. A.; Nuzzo, R. G. Nanostructured Plasmonic Sensors. *Chem. Rev.* **2008**, *108*, 494–521.
4. Ebbesen, T. W.; Lezec, H. J.; Ghaemi, H. F.; Thio, T.; Wolff, P. A. Extraordinary Optical Transmission through Subwavelength Hole Arrays. *Nature* **1998**, *391*, 667–669.
5. Kawata, S. Near-Field Optics and the Surface Plasmon Polariton. In *Near-Field Optics and Surface Plasmon Polaritons*; Springer-Verlag: New York, 2001; pp 1−13.
6. Lezec, H. J.; Degiron, A.; Devaux, E.; Linke, R. A.; Martin-Moreno, L.; Garcia-Vidal, F. J.; Ebbesen, T. W. Beaming Light from a Subwavelength Aperture. *Science* **2002**, *297*, 820–822.
7. Anker, J. N.; Hall, W. P.; Lyandres, O.; Shah, N. C.; Zhao, J.; Van Duyne, R. P. Biosensing with Plasmonic Nanosensors. *Nat. Mater.* **2008**, *7*, 442–453.
8. Brolo, A. G.; Gordon, R.; Leathem, B.; Kavanagh, K. L. Surface Plasmon Sensor Based on the Enhanced Light Transmission through Arrays of Nanoholes in Gold Films. *Langmuir* **2004**, *20*, 4813–4815.
9. Tetz, K. A.; Pang, L.; Fainman, Y. High-Resolution Surface Plasmon Resonance Sensor Based on Linewidth-Optimized Nanohole Array Transmittance. *Opt. Lett.* **2006**, *31*, 1528–1530.
10. Yang, J. C.; Ji, J.; Hogle, J. M.; Larson, D. N. Metallic Nanohole Arrays on Fluoropolymer Substrates as Small Label-Free Real-Time Bioprobes. *Nano Lett.* **2008**, *8*, 2718–2724.
11. Gordon, R.; Sinton, D.; Kavanagh, K. L.; Brolo, A. G. A New Generation of Sensors Based on Extraordinary Optical Transmission. *Acc. Chem. Res.* **2008**, *41*, 1049–1057.
12. Lee, K. L.; Lee, C. H.; Wang, W. S.; Wei, P. K. Sensitive Biosensor Array by Using Surface Plasmon Resonance on Metallic Nanoslits. *J. Biomed. Opt.* **2007**, *12*, 044023.
13. Lee, K. L.; Wang, W. S.; Wei, P. K. Sensitive Label-Free Biosensors by Using Gap Plasmons in Gold Nanoslits. *Biosens. Bioelectron.* **2008**, *24*, 210–215.
14. Lee, K. L.; Wu, S. H.; Wei, P. K. Intensity Sensitivity of Gold Nanostructures and Its Application for High-Throughput Biosensing. *Opt. Express* **2009**, *17*, 23104–23113.
15. Lee, K. L.; Wei, P. K. Enhancing Surface Plasmon Detection Using Ultrasmall Nanoslits and a Multispectral Integration Method. *Small* **2010**, *6*, 1900–1907.
16. Schena, M.; Shalon, D.; Davis, R. W.; Brown, P. O. Quantitative Monitoring of Gene Expression Patterns with a Complementary DNA Microarray. *Science* **1995**, *270*, 467–470.
17. MacBeath, G; Schreiber, S. L. Printing Proteins as Microarrays for High-Throughput Function Determination. *Science* **2000**, *289*, 1760–1763.
18. Fano, U. The Theory of Anomalous Diffraction Gratings and of Quasi-Stationary Waves on Metallic Surfaces (Sommerfeld's Waves). *J. Opt. Soc. Am.* **1941**, *31*, 213–222.
19. Hessel, A.; Oliner, A. A. A New Theory of Wood's Anomalies on Optical Gratings. *Appl. Opt.* **1965**, *4*, 1275–1297.
20. Miroshnichenko, A. E.; Flach, S.; Kivshar, Y. S. Fano Resonances in Nanoscale Structures. *Rev. Mod. Phys.* **2010**, *82*, 2257–2298.

21. Menezes, J. W.; Ferreira, J.; Santos, M. J. L.; Cescato, L.; Brolo, A. G. Large-Area Fabrication of Periodic Arrays of Nanoholes in Metal Films and Their Application in Biosensing and Plasmonic-Enhanced Photovoltaics. *Adv. Funct. Mater.* **2010**, *20*, 3918–3924.
22. Stewart, M. E.; Mack, N. H.; Malyarchuk, V.; Soares, J. A. N. T.; Lee, T. W.; Gray, S. K.; Nuzzo, R. G.; Rogers, J. A. Quantitative Multispectral Biosensing and 1D Imaging Using Quasi-3D Plasmonic Crystals. *Proc. Natl. Acad. Sci. U.S.A.* **2006**, *103*, 17143–17148.
23. Lee, S. H.; Bantz, K. C.; Lindquist, N. C.; Oh, S. H.; Haynes, C. L. Self-Assembled Plasmonic Nanohole Arrays. *Langmuir* **2009**, *25*, 13685–13693.
24. Henzie, J.; Lee, M. H.; Odom, T. W. Multiscale Patterning of Plasmonic Metamaterials. *Nat. Nanotechnol.* **2007**, *2*, 549–554.
25. Nagpal, P.; Lindquist, N. C.; Oh, S. H.; Norris, D. J. Ultrasmooth Patterned Metals for Plasmonics and Metamaterials. *Science* **2009**, *325*, 594–597.
26. Chen, K. P.; Drachev, V. P.; Borneman, J. D.; Kildishev, A. V.; Shalaev, V. M. Drude Relaxation Rate in Grained Gold Nanoantennas. *Nano Lett.* **2010**, *10*, 916–922.
27. Hegner, M.; Wagner, P.; Semenza, G. Ultralarge Atomically Flat Template-Stripped Au Surfaces for Scanning Probe Microscopy. *Surf. Sci.* **1993**, *291*, 39–46.
28. Im, H.; Lee, S. H.; Wittenberg, N. J.; Johnson, T. W.; Lindquist, N. C.; Nagpal, P.; Norris, D. J.; Oh, S. H. Template-Stripped Smooth Ag Nanohole Arrays with Silica Shells for Surface Plasmon Resonance Biosensing. *ACS Nano* **2011**, *5*, 6244–6253.
29. Lindquist, N. C.; Johnson, T. W.; Norris, D. J.; Oh, S. H. Monolithic Integration of Continuously Tunable Plasmonic Nanostructures. *Nano Lett.* **2011**, *11*, 3526–3530.
30. Gordon, R. Light in a Subwavelength Slit in a Metal: Propagation and Reflection. *Phys. Rev. B* **2006**, *73*, 153405.
31. Lee, K. L.; Wei, P. K. Optimization of Periodic Gold Nanostructures for Intensity-Sensitive Detection. *Appl. Phys. Lett.* **2011**, *99*, 083108.
32. Sherry, L. J.; Chang, S. H.; Schatz, G. C.; Van Duyne, R. P.; Wiley, B. J.; Xia, Y. N. Localized Surface Plasmon Resonance Spectroscopy of Single Silver Nanocubes. *Nano Lett.* **2005**, *5*, 2034–2038.
33. Chen, H.; Kou, X.; Yang, Z.; Ni, W.; Wang, J. Shape- and Size-Dependent Refractive Index Sensitivity of Gold Nanoparticles. *Langmuir* **2008**, *24*, 5233–5237.
34. Hao, F.; Sonnefraud, N.; Van Dorpe, P.; Maier, S. A.; Halas, N. J.; Nordlander, P. J. Symmetry Breaking in Plasmonic Nanocavities: Subradiant LSPR Sensing and a Tunable Fano Resonance. *Nano Lett.* **2008**, *8*, 3983–3988.
35. Mirin, N. A.; Bao, K.; Nordlander, P. Fano Resonances in Plasmonic Nanoparticle Aggregates. *J. Phys. Chem. A* **2009**, *113*, 4028–4034.
36. Liu, N.; Weiss, T.; Mesch, M.; Langguth, L.; Eigenthaler, U.; Hirscher, M.; Sonnichsen, C.; Giessen, H. Planar Metamaterial Analogue of Electromagnetically Induced Transparency for Plasmonic Sensing. *Nano Lett.* **2010**, *10*, 1103–1107.
37. Verellen, N.; Van Dorpe, P.; Huang, C. J.; Lodewijks, K.; Vandenbosch, G. A. E.; Lagae, L.; Moshchalkov, V. V. Plasmon Line Shaping Using Nanocrosses for High Sensitivity Localized Surface Plasmon Resonance Sensing. *Nano Lett.* **2011**, *11*, 391–397.
38. Pang, L.; Hwang, G. M.; Slutsky, B.; Fainman, Y. Spectral Sensitivity of Two-Dimensional Nanohole Array Surface Plasmon Polariton Resonance Sensor. *Appl. Phys. Lett.* **2007**, *91*, 123112.
39. Chang, W. J.; Wu, J. T.; Lin, K. H.; Yang, S. Y.; Lee, K. L.; Wei, P. K. Fabrication of Gold Sub-Wavelength Pore Array Using Gas-Assisted Hot Embossing with Anodic Aluminum Oxide (AAO) Template. *Microelectron. Eng.* **2011**, *88*, 6909–6913.